Transport measurements in twisted bilayer graphene:
Electron-phonon coupling and Landau level crossing

Ting-Fung Chung,[1,*] Yang Xu,[1] and Yong P. Chen[1,2,3,†]

[1]*Department of Physics and Astronomy and Birck Nanotechnology Center, Purdue University, West Lafayette, Indiana 47907, USA*
[2]*School of Electrical and Computer Engineering and Purdue Quantum Center, Purdue University, West Lafayette, Indiana 47907, USA*
[3]*WPI-AIMR International Research Center on Materials Science, Tohoku University, Sendai 980-8577, Japan*

We investigate electronic transport in twisted bilayer graphene (tBLG) under variable temperatures (T), carrier densities (n), and transverse magnetic fields, focusing on samples with small twist angles (θ). These samples show prominent signatures associated with the van Hove singularities (VHSs) and superlattice-induced minigaps (SMGs). Temperature-dependent field-effect measurement shows that the difference between temperature-dependent resistivity and residual resistivity, $\rho_{xx}(T,n) - \rho_0(n)$, follows $\sim T^\beta$ for n between the main Dirac point (DP) and SMG. The evolution of the temperature exponent β with n exhibits a W-shaped dependence, with minima of $\beta \sim 0.9$ near the VHSs and maxima of $\beta \sim 1.7$ toward the SMGs. This W-shaped behavior can be qualitatively understood with a theoretical picture that considers both the Fermi surface smearing near the VHSs and flexural-acoustic phonon scattering. In the quantum Hall regime, we observe only Landau level crossings in the massless Dirac spectrum originating from the main DP but not in the parabolic band near the SMG. Such crossings enable the measurement of an enhanced interlayer dielectric constant, attributed to a reduced Fermi velocity. Moreover, we measure the Fermi velocity, interlayer coupling strength, VHS energy relative to the DP, and gap size of SMG, four important parameters used to describe the peculiar band structure of the small-θ tBLG.

I. INTRODUCTION

Twisted bilayer graphene (tBLG), which can be formed by stacking two graphene crystals with a twist angle (θ), is an important example of moiré crystals [1–8]. The tBLG with small θ is particularly interesting, since the moiré pattern periodicity enlarges and the separation between the van Hove singularity (VHS) and Dirac point (DP) shrinks when reducing θ, yielding dramatic changes to the electronic band structure near the DP. In earlier transport studies [9–12], however, sample disorder and limited tunability in the carrier density (e.g., by $\sim 6 \times 10^{12}$ cm^{-2} for typical SiO$_2$/Si back gates) hindered the investigation of the electrical properties of small-θ tBLG. Recent advances in the accurate manipulation of θ (down to $\leqslant 2°$) and high-quality tBLG samples sandwiched between two layers of hexagonal boron nitride (h-BN) have revealed many intriguing transport features associated with tBLG and its moiré band [3], such as VHSs [13–17], superlattice-induced minigaps (SMGs) [16,17], magnetic-field-induced Hofstadter butterfly spectrum [18], and Fabry-Pérot interferences due to networks of helical states formed between the alternating AB/BA regions in very small-θ tBLG [19,20]. Particularly, recent experiments performed on tBLG near the "magic angle" ($\sim 1.1°$) [21,22] revealed that tBLG can exhibit flat energy band near-charge neutrality and Mott-like insulating states at half filling [21] as well as superconducting domes when the carrier density is slightly away from the half-filled case [22].

Although prominent transport signatures [15–18] related to the VHS and SMG have been reported for h-BN-sandwiched tBLG samples with $\theta \leqslant 2°$, there remain many open questions regarding the transport characteristics of this system. One is that little is known about the electron-phonon (el-ph) coupling as a function of temperature (T) and carrier density (n) for in-plane transport and in particular, how the VHS and SMG alter the el-ph coupling. Acoustic phonon-contributed resistivity and phonon-limited carrier mobility have been extensively studied in monolayer and Bernal (AB)-stacked bilayer graphene [23–26]. However, for tBLG, thus far such experiments have been performed only for interlayer transport and the samples with relatively large θ [27,28]. Another is regarding the measured (transport) gap of SMG. Earlier tBLG devices fabricated on SiO$_2$/Si did not show a minigap [9,11,12], while in the h-BN-encapsulated samples, it has been observed that the gap size of SMG varies widely from $\sim$10–60 meV for $\theta \sim 1.8$–$2°$ [16,17]. Further, the nature of this minigap, which is found to be several times larger than the theoretical prediction [17], remains to be fully understood.

Here, we report a transport study of top- and back-gated tBLG samples with h-BN encapsulation under variable T, n, and magnetic fields (B). In this study, we focus on tBLG with small $\theta \sim 2°$ (but still larger than the magic angle) [21]. Our high-quality tBLG devices, exhibiting notable transport features corresponding to the VHSs and SMGs, confirm the recent finding of relatively large SMG gap, and provide insights into the acoustic phonon scattering and interlayer coupling in the small-θ regime. We observe the T dependence of acoustic phonon-contributed resistivity at various n follows a power law, $\sim T^\beta$. The T-exponent β of the resistivity shows a W-

*Corresponding author: tfchung@lbl.gov
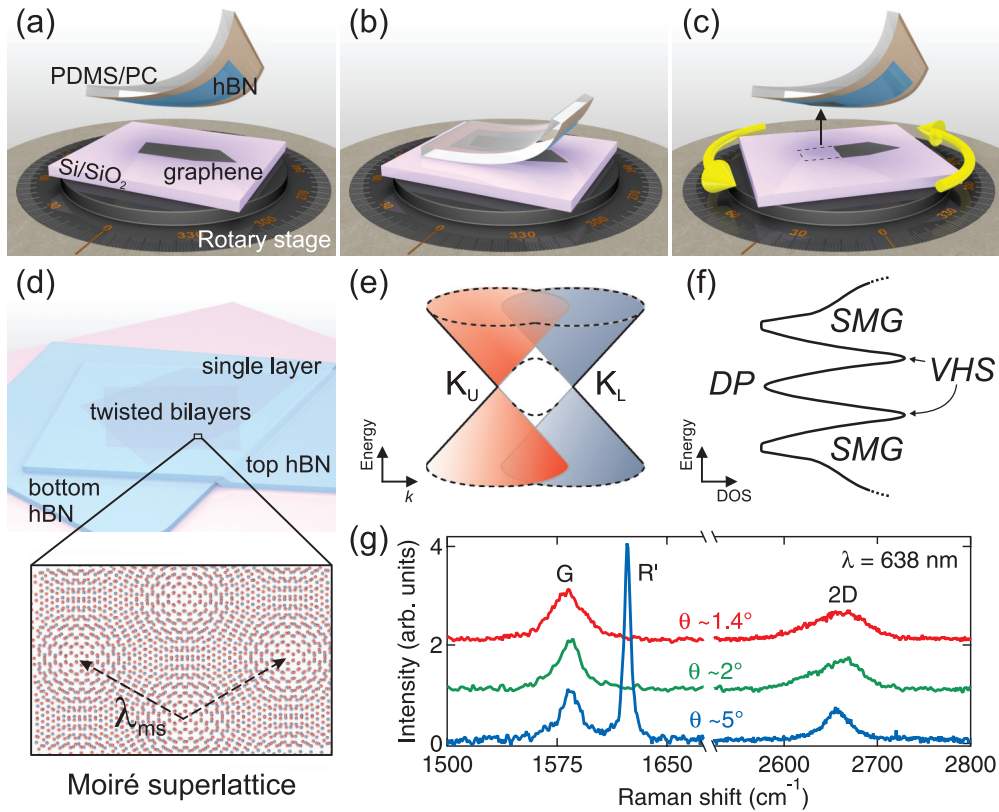†Corresponding author: yongchen@purdue.edu

FIG. 1. (a)–(d) Schematics of our technique for assembling twisted bilayer graphene encapsulated in hexagonal boron nitride, with a controlled twist angle θ between the two monolayers (broken from the same piece of graphene single crystal). The inset below (d) shows the moiré superlattice of tBLG with a lattice constant λ_{ms}. Sketches of (e) tBLG band structure, showing Dirac cones at K valley of the upper and lower layers with a finite momentum separation, and of (f) its electronic density of states. The hybridization between the two graphene layers yields van Hove singularities and superlattice-induced minigaps. The VHSs and SMGs are situated away from the charge-neutrality point and the main Dirac point of each Dirac cone. (g) Raman spectra of tBLG samples with θ of 1.4°, 2°, and 5°. Spectra are individually normalized to the intensity of their respective G peak and are shifted vertically for clarity. Data were measured with 638-nm laser excitation.

shaped n dependence and evolves from $\sim$0.9 to $\sim$1.7 when tuning n away from the VHS. Additionally, as we adjust the transverse electric field (interlayer potential) in the samples in the quantum Hall (QH) regime, a mapping of the Landau quantization shows crossings of two sets of Landau levels (LLs) for n below the VHS but only one set of LLs (no crossing) for n beyond the VHS. By analyzing the electric-field-induced LL crossings, we find enhanced interlayer screening in tBLG (the interlayer dielectric constant is $\sim$6 times the vacuum permittivity), which is understood as a consequence of the reduced Fermi velocity (v_F) due to the interlayer interaction. We also deduce the interlayer coupling strength, VHS energy (E_{VHS}, the energy difference between the main DP and VHS), SMG gap size, and the reduced v_F, revealing strong interlayer coupling in our h-BN-sandwiched tBLG and providing an interpretation consistent with recent scanning tunneling microscopy (STM) findings [15,29] and calculations [15,30].

II. RESULTS AND DISCUSSION

Our samples consist of h-BN/tBLG/h-BN stacks, focusing on small θ around 1.3–2°, and an intermediate $\theta \sim 5°$ as a reference. We assembled tBLG using the dry transfer method [31,32]. The angle alignment was achieved by breaking and stacking from the same large piece of single-crystal graphene

flake (exfoliated from kish graphite from Covalent Materials Corp.) on a rotary stage with angular accuracy $\sim$0.1°, as depicted in Figs. 1(a)–1(d). Figure 1(g) shows representative Raman spectra (measured with a 638-nm laser excitation) of three samples ($\theta \sim$1.4°, 2°, and 5°) before thermal annealing (postannealed samples used in our devices show noisier, but qualitatively similar Raman spectra). We observe a broadening of the G band and an asymmetric 2D band when reducing θ, similar to the prior report in double-layer graphene [using stacks of chemical vapor deposition (CVD)-grown graphene] [33]. These θ-dependent Raman features indicate the tBLG samples with a relatively small θ (accurate determination of θ is by transport measurement as described in Fig. 2) [33]. The stack is patterned into an edge-contacted device [31]. The device has both top and back gates for controlling the total carrier density $n = n_L + n_U$ (where n_L and n_U are the carrier density of the lower and upper graphene layers, respectively) and the average displacement field (applied normal to the layers) D between the two layers. By adjusting both gates, we can separately tune $n = (C_B \Delta V_{BG} + C_T \Delta V_{TG})/e$ and $D = (C_B \Delta V_{BG} - C_T \Delta V_{TG})/2$, where $C_{T(B)}$ is the capacitance per unit area of the top- (back-) gate dielectric, $e = 1.602 \times 10^{-19}$ C is the elementary charge, $\Delta V_{T(B)G} = V_{T(B)G} - V^{\circ}_{T(B)G}$, $V_{T(B)G}$ is the applied top- (back-) gate voltage, and (V°_{TG}, V°_{BG}) are the gate voltages when both upper and lower
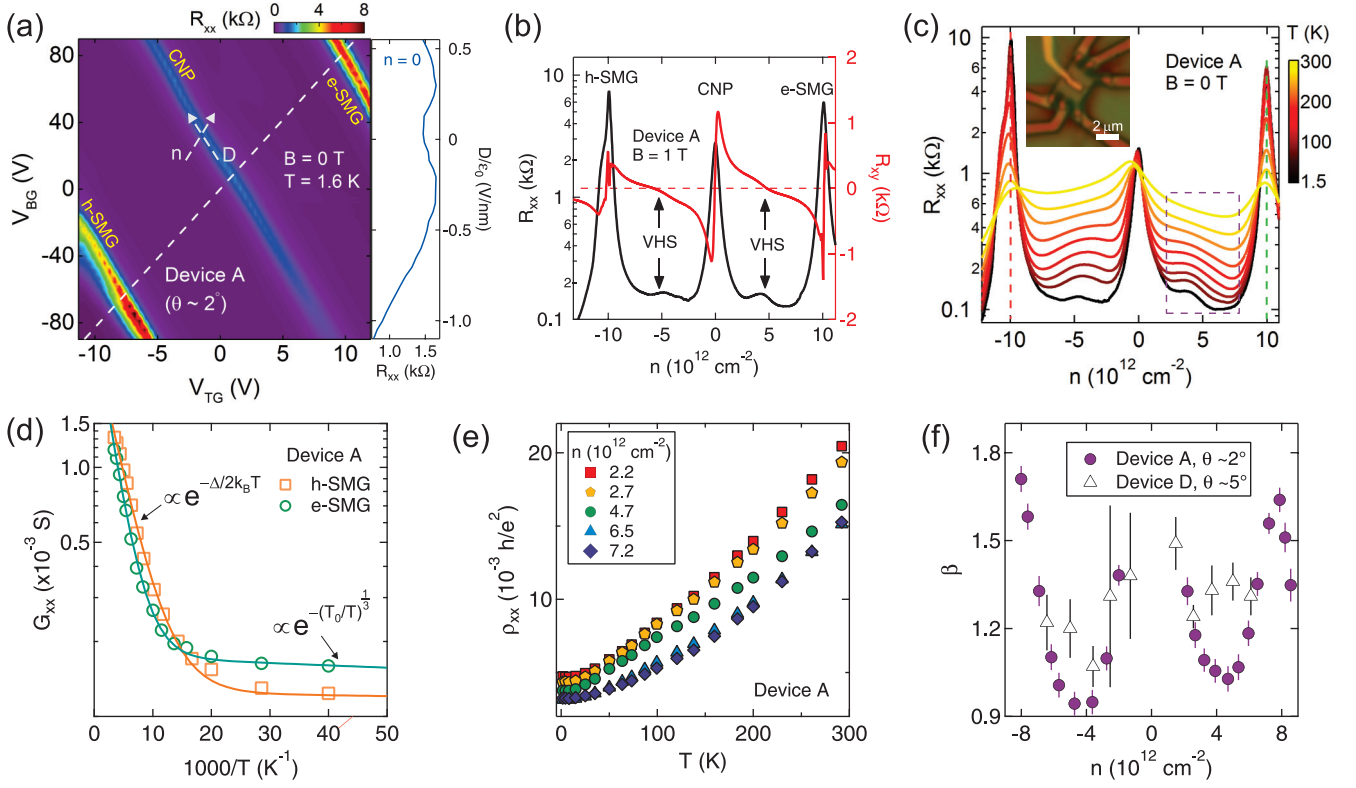
FIG. 2. (a) Longitudinal resistance (R_{xx}) (color scale) as a function of top-gate voltage (V_{TG}) and back-gate voltage (V_{BG}) for tBLG Device A with $\theta \sim 2°$ measured at zero magnetic field ($B = 0$ T) and temperature (T) of 1.6 K. There are two dashed arrows, indicating the axes of n and D (total carrier density and average displacement field applied normal to the graphene layers; see also the definition in the main text). Along the n axis, $D = 0$ when there is no interlayer voltage difference [the Dirac cones in the two layers are aligned in energy; see Fig. 1(e)], while along the D axis, $n = 0$ when the total carrier density in the two layers is zero. The inset shows R_{xx} extracted along $n = 0$ (along the central blue stripe in the main panel) versus D/ε_0. (b) R_{xx} (in log scale) and Hall resistance (R_{xy}) of Device A measured as functions of n along the dashed line in (a) by tuning V_{TG} and V_{BG} simultaneously at $B = 1$ T and $T = 1.6$ K. Sign reversal in the R_{xy} at CNP, VHSs, and SMGs indicates a change in charge carrier type (from electron to hole or vice versa). The two shallow resistance peaks in R_{xx} correspond to the two VHSs, where R_{xy} also crosses zero. (c) R_{xx} (at $B = 0$ T) of Device A as a function of n along the dashed line in (a) at various T, showing the insulating behavior around $n = n_s = \pm 9.9 \times 10^{12}$ cm^{-2}, from which the twist angle θ is estimated. The inset shows an optical image of device A. (d) Arrhenius plot of the conductance ($G_{xx} = 1/R_{xx}$) extracted at n_s for the SMGs. The solid lines are fits to $G_{xx} = G_{TA} \exp(-\Delta/2k_BT) + G_{VRH}\exp[-(T_0/T)^{1/3}]$ (see the main text for details). The activation gap (Δ) is $\sim$65 meV and $\sim$45 meV for the electron- and hole-side minigaps, respectively. (e) T dependence of resistivity (ρ_{xx}) for n from 2.2 to 7.2×10^{12} cm^{-2}, in the range marked by the dashed rectangle in (c), exhibiting metallic behavior ($d\rho_{xx}/dT > 0$). The T dependence below $\sim$150 K can be fitted to $\Delta\rho_{xx}(T,n) = \rho_{xx}(T,n) - \rho_0(n) = \alpha T^\beta$, attributed to acoustic phonon scattering. (f) Fitted T-exponent (β) as a function of n for Devices A ($\theta \sim 2°$) and D ($\theta \sim 5°$).

graphene layers are charge neutral, and $D = 0$ indicates $n_L = C_B \Delta V_{BG}/e = C_T \Delta V_{TG}/e = n_U$. The simple approximations for n and D above are good because the quantum capacitance of doped graphene is at least an order of magnitude larger than the gate capacitance (with the h-BN layer as a gate dielectric) and thus can be neglected. In Device A [see Fig. 2(a)], for example, we obtain $V_{TG}^\circ = -1.45$ V and $V_{BG}^\circ = 32.8$ V (corresponding to the intersection of the two dashed arrows indicating axes of n and D). The gate capacitances are calculated from the thicknesses of h-BN and SiO$_2$ and are confirmed with gate-dependent Hall measurements. Details of sample preparation and device fabrication are in see Supplemental Material [34].

We focus on Device A ($\theta \sim 2°$), which shows a Hall mobility $\sim$25,000 cm^2 V^{-1} s^{-1} for $n \approx 1.5 \times 10^{12}$ cm^{-2} at $T = 1.6$ K. A measurement of the (four-terminal) longitudinal resistance (R_{xx}) versus V_{TG} and V_{BG} is shown in the color plot in Fig. 2(a), taken at $B = 0$ T and $T = 1.6$ K. The central blue stripe denotes the resistance peak of total charge-neutrality

point (CNP) in which both layers have equal and opposite carrier densities such that the tBLG maintains charge neutral (total $n = 0$). The resistance of the central CNP as a function of D/ε_0 (with ε_0 being the vacuum permittivity) is displayed in the inset, showing that the resistance is reduced by a factor of $\sim$2 as D increases, similar to that in large-θ tBLG (see Ref. [35]). In addition to the central CNP, two parallel red stripes (which are relatively insulating) away from the CNP are e-SMG and h-SMG (here, e- and h denote electron- and hole-side, respectively) [16,17]. The resistance of the SMG is tunable by D/ε_0, as depicted in the h-SMG with reducing resistance (color from red to yellow) at larger D. This reduction in the resistance of SMG with D could be understood as a result of lifting the subband degeneracy due to the interlayer potential [36].

Figure 2(b) presents R_{xx} and the Hall resistance (R_{xy}) measured as functions of n along the dashed line in (a) at $B = 1$ T and $T = 1.6$ K. We observe three abrupt zero crossings in R_{xy}, where R_{xx} also reaches maximum, at $n = 0$

and $n = n_s \approx \pm 9.9 \times 10^{12}\,\mathrm{cm}^{-2}$ [corresponding to CNP and SMGs, respectively, represented by the blue stripe and two red stripes in (a)]. The gradual sign reversal in R_{xy} at $n = n_{\mathrm{VHS}} \approx \pm 5 \times 10^{12}\,\mathrm{cm}^{-2}$ accompanied by a shallow resistance peak in R_{xx} are attributed to the VHS. From the carrier density (n_s) at SMG [8], we can estimate the superlattice unit-cell area $A_{\mathrm{ms}} = 4/n_s \approx 40.4\,\mathrm{nm}^{-2}$ and the superlattice wavelength $\lambda_{\mathrm{ms}} = (2A_{\mathrm{ms}}/\sqrt{3})^{1/2} \approx 6.8\,\mathrm{nm}$. According to $\lambda_{\mathrm{ms}} = \frac{a}{2\sin(\theta/2)}$, where $a = 0.246\,\mathrm{nm}$ is the lattice constant of graphene, we obtain $\theta \sim 2°$ (consistent with the intended value in the fabrication and the estimate based on the Raman measurement). Our device has a notably different resistance of SMG compared to the devices of similar θ ($\sim 2°$) in recent studies [16,17].

Figure 2(c) displays T dependence of R_{xx} (at $B = 0\,\mathrm{T}$) for Device A measured along the dashed line in (a). Note that a small variation of D is present along the dashed line due to limitations in the gate voltage to access both SMGs. The resistance of both SMGs increases by about an order of magnitude, accompanied by a narrowing of the resistance peak, as T decreases from 300 to 40 K. We extract the resistance of both SMGs at $\pm n_s$ for various T and plot the log of conductance ($G_{xx} = 1/R_{xx}$) versus $1/T$, as shown in Fig. 2(d). The h-SMG's G_{xx} (open squares) decreases slightly faster than that for the e-SMG (open circles), but both appear to begin saturating below ~ 30 K. It is evident that the SMG's G_{xx} above 120 K follow the thermally activated behavior, $G_{xx} \propto \exp(-\Delta/2k_{\mathrm{B}}T)$, where Δ is the thermal activation (TA) gap, k_{B} is the Boltzmann constant. At lower T, the deviation from the thermally activated transport to the much weaker T dependence is attributed to the Mott variable range hopping (VRH) conduction mediated by localized states. These localized states are attributed to disorder, as indicated by the limited Hall mobility, and to adjacent high-energy bands accessible by phonon-assisted indirect transitions [16,27,37]. We thus add an extra term to represent the Mott VRH conductance and fit our data (over the temperature range between 15 and 300 K) to $G_{xx} = G_{\mathrm{TA}}e^{-\Delta/2k_{\mathrm{B}}T} + G_{\mathrm{VRH}}e^{-(T_o/T)^{1/\beta}}$, where G_{TA} and G_{VRH} are the prefactors of TA and VRH terms, respectively, and T_o is the characteristic temperature for VRH. For the e- and h-SMGs, we find $\Delta \sim 65$ and ~ 45 meV, respectively. We measured Δ (~ 52 to 79 meV) in two more devices with $\theta < 2°$.

Recent reports on small-θ tBLG have found a range of Δ for the superlattice-induced insulating behavior. Our experimentally measured Δ are comparable to the results (50–60 meV) reported in Ref. [17], which are 5–10 times higher than those in earlier experiments and theoretical calculations [16,17]. Several reasons have been proposed to explain this surprisingly large Δ measured in experiments (nearly ~ 10 times larger than the calculated Δ), such as the formation of domains of different stacking and lattice deformation (strain), buckling effect, many-body interactions, and underestimated interlayer coupling strength (t_θ) [17,38,39]. We rule out the unexpectedly large t_θ from our analysis of magnetotransport measurements discussed below. The obtained t_θ is found to be comparable to previous calculations and STM results [1,12,29,40]. Precise causes for the large Δ remain to be better understood.

Figure 2(e) shows T dependence of the longitudinal resistivity (ρ_{xx}, sheet resistivity) for several n between the CNP and e-SMG, corresponding to the range marked by the dashed rectangle in Fig. 2(c). We find that for each measured n between 2×10^{12} and $8 \times 10^{12}\,\mathrm{cm}^{-2}$, $\rho_{xx}(T)$ decreases with decreasing T (metallic behavior, $d\rho_{xx}/dT > 0$, attributed to acoustic phonon scattering) and saturates (below 20 K) to a residual value $\rho_0(n) \sim (115 \pm 35)\,\Omega$ [or $(4.5 \pm 1.3) \times 10^{-3}\,\mathrm{h}/e^2$], attributed to charged impurity scattering. The observed metallic behavior is n dependent, showing a different rate of resistivity increase with increasing T. In contrast to the tBLG, monolayer graphene exhibits a linear temperature dependence in resistivity ($\rho_{xx} \propto T$), independent of n, and AB-bilayer graphene shows very weak T dependence over comparable n ranges as we measured [25,41]. We have also examined T-dependent ρ_{xx} of the reference Device D ($\theta \sim 5°$). The Dirac cones of those bilayers are displaced by a large wave vector in momentum space and mostly decoupled. Hence, the VHSs ($\pm n_{\mathrm{VHS}}$) of such samples are out of the range of accessible n. In Device A, we find that the room-temperature resistivity is higher than the low-T saturation value by $\rho_{xx}(n, T = 300\,\mathrm{K}) - \rho_0(n) \sim 300 - 500\,\Omega/\square$, attributed to the contribution due to electron-acoustic phonon scattering. In contrast, $\rho_{xx}(n, T = 300\,\mathrm{K}) - \rho_0(n)$ is only $\sim 30\,\Omega/\square$ in Device D over comparable ranges of n. This difference may be attributed to that Device D has a larger separation of the Dirac cones from the upper and lower graphene layers in momentum space, $\Delta K = 2|\Gamma K|\sin(\theta/2)$, with $\Gamma K = 1.703\,\text{\AA}^{-1}$ being the distance between the Γ and K points of the graphene Brillouin zone, thus requiring phonons with larger momentum (compared to Device A) to couple electrons between the layers.

To quantitatively discern the difference in the resistivity of the tBLG at various n, we fit the $\rho_{xx}(T < \sim 150\,\mathrm{K})$ data to $\Delta\rho_{xx} = \rho_{xx}(n, T) - \rho_0(n) = \alpha T^\beta$, where α is the prefactor and β is the T exponent. Figure 2(f) presents β versus n for Devices A ($\theta \sim 2°$) and D ($\theta \sim 5°$). The β value of Device A displays a W-shaped curve with minima of ~ 0.9 at $\pm n_{\mathrm{VHS}}$ and maxima of $\sim 1.4 - 1.6$ when n approaches $\pm n_{\mathrm{SMG}}$, whereas for Device D, β ranges from ~ 1 to 1.3 and does not show a strong dependence on n. Note that the measured β differs from that in monolayer graphene, in which the in-plane acoustic (LA/TA) phonon scattering gives rise to a linear-in-T resistivity ($\beta \approx 1$) [23,25]. The resistivity of tBLG, however, can be significantly affected by both interlayer scattering via flexural phonons and intralayer scattering via in-plane acoustic phonons [27,37,42,43], leading to $\beta > 1$, as observed in Devices A and D (in the regime of two decoupled monolayers). While one might expect similar phonon-scattering scenarios for both devices, the characteristic band structure of tBLG in the regime of small θ as in Device A could markedly affect the resistivity. Near the VHSs, a suppression of v_{F} caused by the interlayer coupling [43] leads to a rise in the resistivity, manifested as the small and broad peaks located at $\sim \pm n_{\mathrm{VHS}}$, as shown in Fig. 2(c). At higher T, thermal broadening [43] smears out these resistivity peaks and decreases β to ~ 0.9. Theories [37,43] have considered different contributions of acoustic phonon modes to the el-ph scattering in tBLG at various θ. The theories [37,43] have predicted a significant change in the contribution of different phonon modes to the resistivity when n increases toward SMG in the small-θ regime, which may offer an interpretation for the distinct n dependence of β [Fig. 2(f)] we observed in Devices A and D.
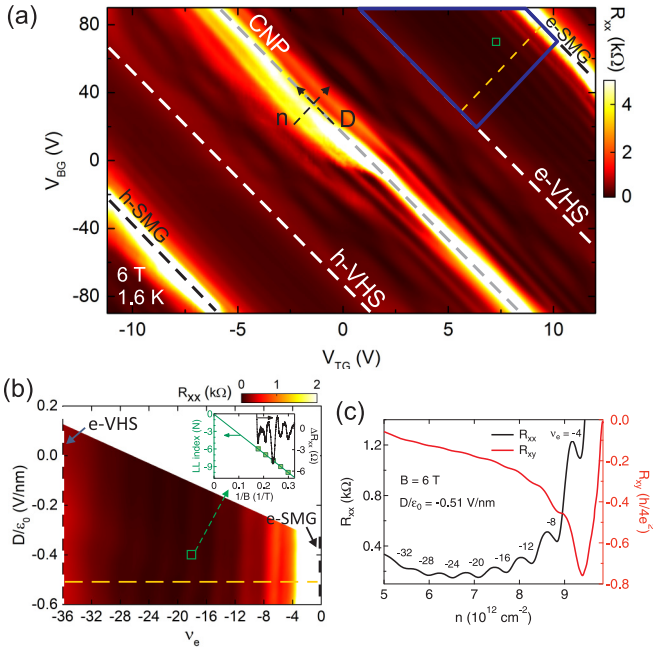
FIG. 3. (a) Longitudinal resistance (R_{xx}) (color scale) as a function of V_{TG} and V_{BG} for Device A, measured at $B = 6$ T and $T = 1.6$ K. For carrier density n between the two VHSs, we observe crossing of two sets of Landau levels when the layer degeneracy is broken by applying D. In contrast, only one set of LLs (manifested as lines parallel to the D axis) are observed for n beyond those of the VHS in the electron- or hole-side of CNP. (b) Zoomed-in color-scale plot of the R_{xx} (from the region bounded by blue solid lines in (a), between the VHS and SMG in the electron side of CNP) as a function of D/ε_0 and filling factor (ν_e, measured from the e-SMG), showing developing quantum Hall states (occurring in steps of 4 in ν_e). The inset shows the assigned LL index (N) and corresponding SdH oscillations in ΔR_{xx} (R_{xx} with background subtracted) versus $1/B$, taken at fixed gate voltages [marked by the green open square in (a), (b)] with $D/\varepsilon_0 \sim -0.4$ V/nm and $n - n_{e-SMG} = -3.2 \times 10^{12}$ cm^{-2} (measured from the e-SMG; the negative sign represents holelike carriers). The solid line is a linear fit with N-axis intercept -0.07 ± 0.05, indicating zero Berry phase (different from the massless charge carriers in monolayer). (c) R_{xx} and R_{xy} versus n at $D/\varepsilon_0 = -0.51$ V/nm, measured along the orange dashed line in (a), (b).

We have also measured quantum Hall effects in such small-θ tBLG samples as Device A and found features different from those in either AB-bilayer or large-θ tBLG [35,44]. Figure 3(a) presents a color plot of R_{xx} versus V_{BG} and V_{TG} for Device A, acquired at $B = 6$ T and $T = 1.6$ K. The central and side white stripes represent the CNP and SMGs, located at the same positions as those shown in Fig. 2(a) measured at $B = 0$ T. In the plot, we can observe two markedly different types of LL-like structures originating from the CNP (total $n = 0$) and the side SMGs, separated by the VHSs (white dashed lines). As we will discuss in the following, the LL crossings observed in the vicinity of CNP (between e-VHS and h-VHS) stem from two sets of LLs of the graphene bilayers when D lifts the layer degeneracy, similar to that observed in large-θ tBLG [35]. On the other hand, we observe only one set of LLs that manifests as lines parallel to those corresponding to CNP and SMG [dashed lines in Fig. 3(a)], for n beyond e- or h-VHS.

The zoomed-in resistance map R_{xx} ($B = 6$ T) from the region enclosed by the blue solid lines in (a) is shown in Fig. 3(b). The gate voltages are converted to D/ε_0 and filling factor (measured from the e-SMG) $\nu_e = (n - n_{e-SMG})h/eB$, where h is Planck's constant. The negative values of ν_e in Fig. 3(b) denote holelike carriers between e-SMG and e-VHS [also see R_{xy} in Fig. 2(b)]. We observe the sequence of the QH states (black stripes) following steps of 4 in ν_e (i.e., -4, -8, -12, ...), which is independent of D. Figure 3(c) displays the R_{xx} and R_{xy} as functions of n at $B = 6$ T, measured along the orange dashed line with $D/\varepsilon_0 = -0.51$ V/nm in (b). R_{xy} exhibits several developing quantized plateaus at $-h/8e^2$, $-h/12e^2$, $-h/16e^2$, accompanied by minima in R_{xx}. The ν_e sequence indicates massive fermions (attributed to the parabolic bands around the e-SMG at the Γ_s point of the superlattice Brillouin zone [16,17]) and the fourfold degenerate LLs, which follow from the spin degeneracy and "Fermi contour degeneracy" of the parabolic energy band near the e-SMG [16,17]. We also measure Shubnikov-de Haas (SdH) oscillations at fixed gate voltages [denoted by the green open square in both (a) and (b)], as shown in the inset of (b). The Landau plot [LL index (N) vs $1/B$] of the oscillations in the inset reveals a zero N intercept. This is an indication of zero Berry phase, which is another key feature that is different from the massless charge carriers in monolayer graphene.

We now turn to the CNP region ($n \sim 0$), showing LL crossings emanated from the lower and upper graphene layers. Figure 4(a) displays the zoomed-in color plot of R_{xx} ($B = 6$ T) between the two VHSs (white dashed lines) in Fig. 3(a) as a function of D/ε_0 and $\nu = (n/B)h/e$. The filling-factor combination $\nu = \nu_L + \nu_U$ for several expected QH states (regions in black) has been labeled as a guide to the eye. The subscripts L and U represent lower and upper graphene layers, respectively. A complete set of ν for all expected QH states (according to Ref. [36]) is schematically illustrated in Fig. 4(b). Figure 4(c) presents the R_{xx} and R_{xy} versus n measured at $D = 0$ [along the orange dashed line in (a)]. We observe developing quantized plateaus in R_{xy} at $\pm h/\nu e^2$ for $\nu = 4$, 12, 20, 28 (with steps of 8), consistent with the ν assignment for both electron ($+$ sign) and hole ($-$ sign) doping in (b). This eightfold degeneracy arises from the spin, valley, and layer degeneracies of two monolayers [35]. A similar set of developing plateaus in R_{xy} is observed in the magnetic-field-dependent data at $D = 0$ and $n = 2.4 \times 10^{12}$ cm^{-2}, as in Fig. 4(d). We assign each minimum in R_{xx} of the oscillations to its corresponding $\nu = 8(N + 1/2)$, where $N = 0, \pm1, \pm2, \ldots$ is the index of the filled LL in each graphene layer (noting the lower and upper graphene layers are degenerate with the same filling at $D = 0$). The data of N vs $1/B$ can be linearly fitted with slope 12.7 T and intercept ~ -0.5 in the vertical N axis [see the inset in Fig. 4(d)], revealing a Berry phase π attributed to the decoupled monolayer graphene each possessing a carrier density of $n/2$. On the other hand, we see an alternating stripe pattern (i.e., LL crossing) with changing D in Fig. 4(a), as expected from two decoupled monolayers [10,35]. We further observe a beating pattern in the SdH oscillations at $D/\varepsilon_0 = -1.2$ V/nm [see Fig. 4(e)], confirming a superposition of two independent sets of QH states with different filling factors from the two decoupled monolayers. The inset presents the Fourier transform (FT) amplitude versus frequency corresponding to the data (when plotted
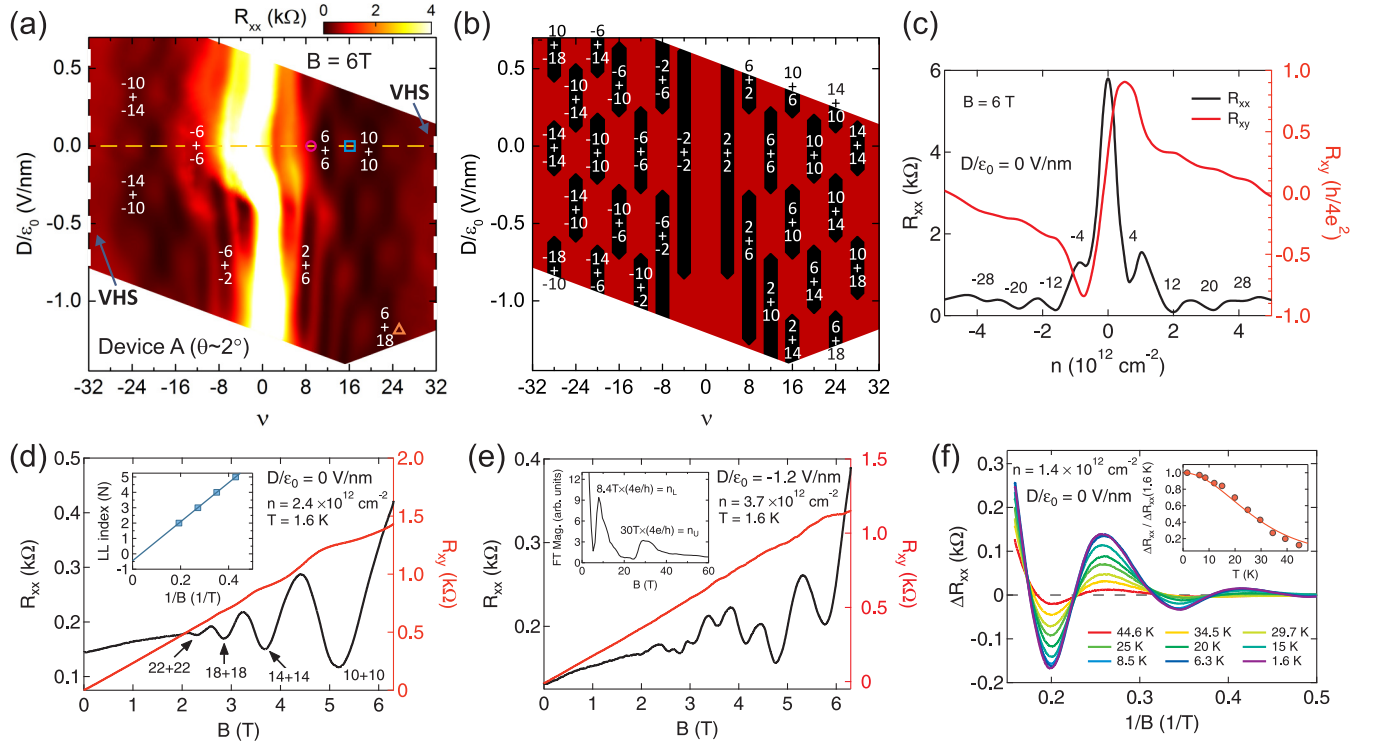
FIG. 4. (a) Close-ups of the R_{xx} (color scale) between the two VHSs in Fig. 3(a) as a function of D/ε_0 and ν, measured at 6 T and 1.6 K. (b) Schematic (adapted from Ref. [36]) of expected QH states (regions in black) with corresponding filling-factor combination ($\nu = \nu_L + \nu_U$) in the measured range in (a). (c) R_{xx} and R_{xy} at $D = 0$, measured along the orange dashed line in (a), as functions of n. The ν associated with the minima in R_{xx} are ± 4, ± 12, ± 20, and ± 28 (indicating eightfold degenerate LL). (d) R_{xx} and R_{xy} as functions of B measured at $D = 0$ and $n = 2.4 \times 10^{12}$ cm^{-2} [marked by the blue open square in (a)], showing SdH oscillations from two decoupled graphene monolayers with the same carrier density ($n/2$). The inset displays the assigned LL index (N) plotted against $1/B$. The solid line is a linear fit with N-axis intercept $+0.49 \pm 0.02$, which indicates π-Berry phase for massless Dirac fermions. (e) R_{xx} and R_{xy} versus B measured at $D/\varepsilon_0 = -1.2$ V/nm and $n = 3.7 \times 10^{12}$ cm^{-2} [marked by the orange open triangle in (a)]. Here the oscillations arise from the two decoupled monolayers, where the layer degeneracy in the LLs (and layer density) has been lifted by $D \neq 0$. The inset shows the magnitude of FT of $R_{xx}(1/B)$. The two peaks at 8.4 and 30 T correspond to the two different layer densities n_U and n_L, respectively. (f) Temperature dependence of the SdH oscillations in ΔR_{xx} (R_{xx} with background subtracted) at $n = 1.4 \times 10^{12}$ cm^{-2} and $D = 0$ [denoted by the pink open circle in (a)]. The inset presents the temperature dependence of the normalized amplitude of ΔR_{xx} for the oscillation at 5 T ($\nu = 6 + 6$ QH state). The solid line is a fit to the Lifshitz-Kosevich formula, yielding the electron effective mass ($m^* \sim 0.029 m_e$) and Fermi velocity ($\nu_F \sim 0.58 \times 10^6$ ms^{-1}).

as R_{xx} vs $1/B$) in Fig. 4(e), exhibiting two prominent peaks arising from the carrier densities of different layers ($n_U \sim 2.9 \times 10^{12}$ cm^{-2} and $n_L \sim 8.1 \times 10^{11}$ cm^{-2}). These results indicate that the low-energy electronic structure ($n < n_{VHS}$) of tBLG ($\theta \sim 2°$) corresponds to that of two decoupled graphene monolayers.

Next, we have performed T-dependent SdH oscillation studies in the decoupled regime in Device A. We estimate the cyclotron mass (m^*) as well as ν_F from the T-dependent oscillations at $n = 1.4 \times 10^{12}$ cm^{-2} and $D = 0$, where the DP of two layers (with comparable doping) is vertically aligned and the band renormalization caused by the interlayer asymmetric potential is negligible [12,45]. Figure 4(f) shows the T dependence of the oscillation amplitude ΔR_{xx} at $n = 1.4 \times 10^{12}$ cm^{-2}. The ΔR_{xx} for the oscillation at 0.2 T^{-1} ($\nu = 6 + 6$ QH state) is normalized by the $\Delta R_{xx}(T = 1.6$ K$)$ and is displayed in the inset as a function of T. By fitting to the Lifshitz-Kosevich formula [46], $\Delta R_{xx}(T,B) \propto [(\chi T/\hbar\omega_c)/\sinh(\chi T/\hbar\omega_c)]e^{-\chi T_D/\hbar\omega_c}$, where χ is a constant, $\hbar\omega_c = \hbar e B/m^*$ and T_D are the fitting parameters, we can extract $m^* \sim 0.029 m_e$ (with m_e being the electron

rest mass) at the Fermi energy. With the Onsager relation, $B_F = A_k(\Phi_0/2\pi^2)$, we can extract the Fermi momentum ($k_F = \sqrt{A_F/\pi}$; a circular Fermi surface A_k of Dirac cone is assumed when the Fermi energy is close to the main CNP and away from VHS) from the SdH oscillation frequency ($B_F \sim 6.85$ T) obtained in Fig. 4(f) and then $\nu_F = \hbar k_F/m^* \sim 0.58 \times 10^6$ ms^{-1}, about a 40% reduction compared with that in monolayer graphene ($\nu_F^0 \approx 10^6$ ms^{-1}). The reduced ν_F is consistent with the finite interlayer coupling in the small-θ tBLG, possessing both low-energy VHSs and SMGs. We also measure a similar $\nu_F \sim (0.56 \pm 0.02) \times 10^6$ ms^{-1} at $n = 2.5 \times 10^{12}$ cm^{-2}. In addition to Device A, we performed similar measurement on Device D (with $\theta \sim 5°$) at similar carrier densities and obtained $\nu_F \sim 1 \times 10^6$ ms^{-1}, comparable to the monolayer graphene value ν_F^0. Our results confirm that ν_F depends strongly on both θ and interlayer coupling in tBLG.

From the reduced ν_F, we can estimate the t_θ and VHS energy (E_{VHS}, the energy difference between the main DP and VHS)— parameters reflecting the interlayer interactions in our tBLG encapsulated in h-BN. It has been shown that ν_F decreases with decreasing θ or increasing interlayer coupling strength (t_θ)

[40], $\nu_F/\nu_F^0 = 1 - 9(t_\theta/\hbar\nu_F^0\Delta K)^2$, where ΔK is the separation between the two DPs (K_L and K_U) in momentum space and $\hbar$ is the reduced Planck constant. For $\theta = 2°$, $\Delta K = 0.059\,\text{Å}^{-1}$, and $\nu_F = 0.58\nu_F^0$, we obtain $t_\theta = (84 \pm 5)\,\text{meV}$, which is in a good agreement with prior theoretical and experimental studies [1,12,15,29,40]. We note the similarity of t_θ measured from small-θ tBLG on different substrates [SiO$_2$ [12] and h-BN (this work)], suggesting that t_θ is relatively insensitive to the surrounding dielectric environment, interfacial strain, and disorder. The energy difference between the two VHSs can be estimated [1] by

$$\Delta E_{VHS} = 2E_{VHS} \approx \hbar\nu_F^0\Delta K - 2t_\theta. \tag{1}$$

By assuming t_θ is comparable in the e-doped and h-doped sides, the equation above yields $\Delta E_{VHS} = 2E_{VHS} \sim 220\,\text{meV}$ and $E_{VHS} \sim 110\,\text{meV}$.

In our experiment, we can also deduce the E_{VHS} from the Landau quantization pattern (R_{xx} vs V_{TG} and V_{BG} at $B = 6\,\text{T}$), as presented in Fig. 3(a). Below the VHSs, the tBLG behaves like two decoupled graphene layers. The LL energy [46] of each monolayer graphene with (reduced) ν_F in perpendicular magnetic field B is given by

$$E_N = \text{sgn}(N)\sqrt{2e\hbar\nu_F^2 B|N|}, \tag{2}$$

where N is the corresponding LL index and the R_{xx} minima would occur at $\nu = 4(N + 1/2)$. As presented in Fig. 3(a), equally spaced lines (passing through points of equal filling factors $\nu = nh/eB = 2, 6, 10 \ldots$ in the two layers) parallel to those corresponding to CNP and VHS can be defined. We find e-VHS is located near $N \sim 3.5$ ($\nu \sim 16$ for monolayer), which yields $E_{VHS} \sim (95 \pm 4)\,\text{meV}$ (calculated from the LL energy expression with a value $\nu_F \sim 0.58\,\nu_F^0$). This is in a reasonable agreement with $E_{VHS} \sim 110\,\text{meV}$ extracted from Eq. (1) above. Our extracted E_{VHS} values are also consistent with a recent STM study of CVD tBLG on h-BN substrate [15].

We further investigate the effect of the reduced ν_F on the interlayer screening of the tBLG. Close to the DP, the density of states vanishes, causing the tBLG to become less efficient in screening adjacent electric fields [47–54]. The incomplete charge screening creates a charge-density imbalance (Δn) as well as an interlayer potential difference (ΔV) between the two graphene layers. The interlayer potential difference with an interlayer spacing (d_{GG}) depends on the difference between the average displacement field (D) and the screening field ($e\Delta n/2$) [35],

$$-\Delta V = (D - e\Delta n/2)/C_{GG}, \tag{3}$$

where $C_{GG} = \varepsilon_0\varepsilon_{GG}/d_{GG}$ is the interlayer capacitance per unit area and ε_{GG} is the interlayer dielectric constant. When two LLs (one from the lower layer with index N_L, the other from the upper layer with index N_U) cross, the LL energy difference ($E_{N_L} - E_{N_U}$) between them provides a measure of

ΔV, $E_{N_L} - E_{N_U} = -e\Delta V$. In addition, the difference between the corresponding LL indices provides a measure of Δn, $\Delta n = (N_L - N_U)4eB/h$. From the values of D, ΔV, and Δn for a given LL crossing, exemplified by those shown in Fig. 4(a), we can extract C_{GG} from Eq. (3). The C_{GG} extracted from several LL crossings studied are in good agreement with each other, with an average $C_{GG} = (17.4 \pm 0.5)\,\mu\text{F/cm}^2$, and corresponding to $\varepsilon_{GG} = 6.7\varepsilon_0$ for $d_{GG} = 0.34\,\text{nm}$. The estimated C_{GG} is at least 2 (7) times of the value in large-θ tBLG (vacuum-filled parallel-plate capacitor with interplate distance d_{GG}) (see Ref. [35]). Such a large C_{GG} is attributed to the reduced ν_F in our small-θ tBLG. We find that the consideration of the effect of quantum capacitance will change the C_{GG} value by $\sim 0.2\,\mu\text{F/cm}^2$, which is smaller than the uncertainty ($\sim 0.5\,\mu\text{F/cm}^2$) in the extracted C_{GG}. Therefore, we ignore the effect of the quantum capacitance in tBLG. The enhancements of C_{GG} and ε_{GG} can also be explained qualitatively by the linear reduction of the Thomas-Fermi screening length with smaller ν_F, $\lambda_{TF} \propto \nu_F/k_F$ (here $k_F = \sqrt{n\pi}$ is the Fermi momentum) [48], indicating a strong electronic screening in the small-θ tBLG.

III. CONCLUSION

In summary, we have performed temperature-dependent and magnetotransport studies on dual-gated tBLG samples with twist angle $\theta \sim 2°$ and encapsulated in h-BN. We have observed the transport features arising from the VHSs and SMGs in addition to the main DP. We have found that the resistivity measured between the CNP ($n \sim 0$) and SMG exhibits a power-law behavior, $\sim T^\beta$. The extracted temperature exponent β features a W-shaped carrier-density dependence with two minima at the VHSs, indicating a distinct electron-phonon coupling for small-θ tBLG. From our experiment, we have measured the SMG gap size, which confirms its relatively large value as reported in a recent study [17]. We have also estimated the interlayer coupling strength, which may be useful for further studies on the origin of the large SMG gap. By measuring quantum oscillations at high magnetic fields, we have observed Berry phase transition from π to 2π when increasing the carrier density and tuning the Fermi level across the VHS. Landau level crossings and Fermi velocity suppression observed at carrier densities below the VHS reveal strong interlayer coupling in the small-θ tBLG.

[1] G. Li, A. Luican, J. M. B. Lopes dos Santos, A. H. Castro Neto, A. Reina, J. Kong, and E. Y. Andrei, Nat. Phys. **6**, 109 (2009).

[2] G. Trambly de Laissardière, D. Mayou, and L. Magaud, Nano Lett. **10**, 804 (2010).

[3] R. Bistritzer and A. H. MacDonald, Proc. Natl. Acad. Sci. USA **108**, 12233 (2011).

[4] M. Yankowitz, J. Xue, D. Cormode, J. D. Sanchez-Yamagishi, K. Watanabe, T. Taniguchi, P. Jarillo-Herrero,

P. Jacquod, and B. J. LeRoy, Nat. Phys. **8**, 382 (2012).

[5] C. R. Dean, L. Wang, P. Maher, C. Forsythe, F. Ghahari, Y. Gao, J. Katoch, M. Ishigami, P. Moon, M. Koshino, T. Taniguchi, K. Watanabe, K. L. Shepard, J. Hone, and P. Kim, Nature (London) **497**, 598 (2013).

[6] L. A. Ponomarenko, R. V Gorbachev, G. L. Yu, D. C. Elias, R. Jalil, A. A. Patel, A. Mishchenko, A. S. Mayorov, C. R. Woods, J. R. Wallbank, M. Mucha-Kruczynski, B. A. Piot, M. Potemski, I. V Grigorieva, K. S. Novoselov, F. Guinea, V. I. Fal'ko, and A. K. Geim, Nature (London) **497**, 594 (2013).

[7] B. Hunt, J. D. Sanchez-Yamagishi, A. F. Young, M. Yankowitz, B. J. LeRoy, K. Watanabe, T. Taniguchi, P. Moon, M. Koshino, P. Jarillo-Herrero, and R. C. Ashoori, Science **340**, 1427 (2013).

[8] Q. Tong, H. Yu, Q. Zhu, Y. Wang, X. Xu, and W. Yao, Nat. Phys. **13**, 356 (2016).

[9] D. S. Lee, C. Riedl, T. Beringer, A. H. Castro Neto, K. von Klitzing, U. Starke, and J. H. Smet, Phys. Rev. Lett. **107**, 216602 (2011).

[10] B. Fallahazad, Y. Hao, K. Lee, S. Kim, R. S. Ruoff, and E. Tutuc, Phys. Rev. B **85**, 201408 (2012).

[11] H. Schmidt, J. C. Rode, D. Smirnov, and R. J. Haug, Nat. Commun. **5**, 5742 (2014).

[12] J. C. Rode, D. Smirnov, H. Schmidt, and R. J. Haug, 2D Mater. **3**, 035005 (2016).

[13] G. Trambly de Laissardière, D. Mayou, and L. Magaud, Phys. Rev. B **86**, 125413 (2012).

[14] S. Shallcross, S. Sharma, and O. Pankratov, Phys. Rev. B **87**, 245403 (2013).

[15] D. Wong, Y. Wang, J. Jung, S. Pezzini, A. M. DaSilva, H.-Z. Tsai, H. S. Jung, R. Khajeh, Y. Kim, J. Lee, S. Kahn, S. Tollabimazraehno, H. Rasool, K. Watanabe, T. Taniguchi, A. Zettl, S. Adam, A. H. MacDonald, and M. F. Crommie, Phys. Rev. B **92**, 155409 (2015).

[16] Y. Kim, P. Herlinger, P. Moon, M. Koshino, T. Taniguchi, K. Watanabe, and J. H. Smet, Nano Lett. **16**, 5053 (2016).

[17] Y. Cao, J. Y. Luo, V. Fatemi, S. Fang, J. D. Sanchez-Yamagishi, K. Watanabe, T. Taniguchi, E. Kaxiras, and P. Jarillo-Herrero, Phys. Rev. Lett. **117**, 116804 (2016).

[18] K. Kim, A. DaSilva, S. Huang, B. Fallahazad, S. Larentis, T. Taniguchi, K. Watanabe, B. J. LeRoy, A. H. MacDonald, and E. Tutuc, Proc. Natl. Acad. Sci. USA **114**, 3364 (2017).

[19] S. Huang, K. Kim, D. K. Efimkin, T. Lovorn, T. Taniguchi, K. Watanabe, A. H. MacDonald, E. Tutuc, and B. J. LeRoy, arXiv:1802.02999.

[20] P. Rickhaus, J. Wallbank, S. Slizovskiy, R. Pisoni, H. Overweg, Y. Lee, M. Eich, M.-H. Liu, K. Watanabe, T. Taniguchi, V. Fal'ko, T. Ihn, and K. Ensslin, arXiv:1802.07317.

[21] Y. Cao, V. Fatemi, A. Demir, S. Fang, S. L. Tomarken, J. Y. Luo, J. D. Sanchez-Yamagishi, K. Watanabe, T. Taniguchi, E. Kaxiras, R. C. Ashoori, and P. Jarillo-Herrero, Nature (London) **556**, 80 (2018).

[22] Y. Cao, V. Fatemi, S. Fang, K. Watanabe, T. Taniguchi, E. Kaxiras, and P. Jarillo-Herrero, Nature (London) **556**, 43 (2018).

[23] E. H. Hwang and S. Das Sarma, Phys. Rev. B **77**, 115449 (2008).

[24] S. V Morozov, K. S. Novoselov, M. I. Katsnelson, F. Schedin, D. C. Elias, J. A. Jaszczak, and A. K. Geim, Phys. Rev. Lett. **100**, 016602 (2008).

[25] J.-H. Chen, C. Jang, S. Xiao, M. Ishigami, and M. S. Fuhrer, Nat. Nanotechnol. **3**, 206 (2008).

[26] E. V. Castro, H. Ochoa, M. I. Katsnelson, R. V. Gorbachev, D. C. Elias, K. S. Novoselov, A. K. Geim, and F. Guinea, Phys. Rev. Lett. **105**, 266601 (2010).

[27] Y. Kim, H. Yun, S.-G. Nam, M. Son, D. S. Lee, D. C. Kim, S. Seo, H. C. Choi, H.-J. Lee, S. W. Lee, and J. S. Kim, Phys. Rev. Lett. **110**, 096602 (2013).

[28] L. Britnell, R. V. Gorbachev, A. K. Geim, L. A. Ponomarenko, A. Mishchenko, M. T. Greenaway, T. M. Fromhold, K. S. Novoselov, and L. Eaves, Nat. Commun. **4**, 1794 (2013).

[29] L.-J. Yin, J.-B. Qiao, W.-X. Wang, W.-J. Zuo, W. Yan, R. Xu, R.-F. Dou, J.-C. Nie, and L. He, Phys. Rev. B **92**, 201408 (2015).

[30] J. Jung, A. Raoux, Z. Qiao, and A. H. MacDonald, Phys. Rev. B **89**, 205414 (2014).

[31] L. Wang, I. Meric, P. Y. Huang, Q. Gao, Y. Gao, H. Tran, T. Taniguchi, K. Watanabe, L. M. Campos, D. A. Muller, J. Guo, P. Kim, J. Hone, K. L. Shepard, and C. R. Dean, Science **342**, 614 (2013).

[32] K. Kim, M. Yankowitz, B. Fallahazad, S. Kang, H. C. P. Movva, S. Huang, S. Larentis, C. M. Corbet, T. Taniguchi, K. Watanabe, S. K. Banerjee, B. J. LeRoy, and E. Tutuc, Nano Lett. **16**, 1989 (2016).

[33] K. Kim, S. Coh, L. Z. Tan, W. Regan, J. M. Yuk, E. Chatterjee, M. F. Crommie, M. L. Cohen, S. G. Louie, and A. Zettl, Phys. Rev. Lett. **108**, 246103 (2012).

[34] See Supplemental Material at http://link.aps.org/supplemental/10.1103/PhysRevB.98.035425 for details of sample fabrication and measurements in more devices different from $2°$. Additional Refs. [50–54] are included in Supplemental Material.

[35] J. D. Sanchez-Yamagishi, T. Taychatanapat, K. Watanabe, T. Taniguchi, A. Yacoby, and P. Jarillo-Herrero, Phys. Rev. Lett. **108**, 076601 (2012).

[36] P. Moon, Y.-W.W. Son, and M. Koshino, Phys. Rev. B **90**, 155427 (2014).

[37] V. Perebeinos, J. Tersoff, and P. Avouris, Phys. Rev. Lett. **109**, 236604 (2012).

[38] S. Dai, Y. Xiang, and D. J. Srolovitz, Nano Lett. **16**, 5923 (2017).

[39] N. N. T. Nam and M. Koshino, Phys. Rev. B **96**, 075311 (2017).

[40] J. M. B. Lopes dos Santos, N. M. R. Peres, and A. H. Castro Neto, Phys. Rev. Lett. **99**, 256802 (2007).

[41] C. R. Dean, A. F. Young, M. C. Lee, L. Wang, S. Sorgenfrei, K. Watanabe, T. Taniguchi, P. Kim, K L. Shepard, and J. Hone, Nat. Nanotechnol. **5**, 722 (2010).

[42] R. He, T.-F. Chung, C. Delaney, C. Keiser, L. A. Jauregui, P. M. Shand, C. C. Chancey, Y. Wang, J. Bao, and Y. P. Chen, Nano Lett. **13**, 3594 (2013).

[43] N. Ray, M. Fleischmann, D. Weckbecker, S. Sharma, O. Pankratov, and S. Shallcross, Phys. Rev. B **94**, 245403 (2016).

[44] K. S. Novoselov, E. McCann, S. V. Morozov, V. I. Fal'ko, M. I. Katsnelson, U. Zeitler, D. Jiang, F. Schedin, and A. K. Geim, Nat. Phys. **2**, 177 (2006).

[45] T.-F. Chung, R. He, T.-L. Wu, and Y. P. Chen, Nano Lett. **15**, 1203 (2015).

[46] Y. Zhang, Y.-W. Tan, H. L. Stormer, and P. Kim, Nature (London) **438**, 201 (2005).

[47] C.-P. Lu, M. Rodriguez-Vega, G. Li, A. Luican-Mayer, K. Watanabe, T. Taniguchi, E. Rossi, and E. Y. Andrei, Proc. Natl. Acad. Sci. USA **113**, 6623 (2016).

[48] A. H. Castro Neto, F. Guinea, N. M. R. Peres, K. S. Novoselov, and A. K. Geim, Rev. Mod. Phys. **81**, 109 (2009).

[49] V. Carozo, C. M. Almeida, E. H. M. Ferreira, L. G. Cançado, C. A. Achete, and A. Jorio, Nano Lett. **11**, 4527 (2011).

[50] M. Zhu, D. Ghazaryan, S.-K. Son, C. R. Woods, A. Misra, L. He, T. Taniguchi, K. Watanabe, K. S. Novoselov, Y. Cao, and A. Mishchenko, 2D Mater. **4**, 011013 (2016).

[51] T. T. Tran, C. Elbadawi, D. Totonjian, C. J. Lobo, G. Grosso, H. Moon, D. R. Englund, M. J. Ford, I. Aharonovich, and M. Toth, ACS Nano **10**, 7331 (2016).

[52] A. G. F. Garcia, M. Neumann, F. Amet, J. R. Williams, K. Watanabe, T. Taniguchi, and D. Goldhaber-Gordon, Nano Lett. **12**, 4449 (2012).

[53] A. Luican, G. Li, A. Reina, J. Kong, R. R. Nair, K. S. Novoselov, A. K. Geim, and E. Y. Andrei, Phys. Rev. Lett. **106**, 126802 (2011).

[54] Y. Kim, J. Park, I. Song, J. M. Ok, Y. Jo, K. Watanabe, T. Taniquchi, H. C. Choi, D. S. Lee, S. Jung, and J. S. Kim, Sci. Rep. **6**, 38068 (2016).